

Nonequilibrium Excitations and Transport of Dirac Electrons in Electric-Field-Driven Graphene

Jiajun Li^{1,2} and Jong E. Han¹

¹*Department of Physics, State University of New York at Buffalo, Buffalo, New York 14260, USA*

²*Department of Physics, Friedrich-Alexander-Universität Erlangen-Nürnberg, Erlangen 91054, Germany*

(Dated: December 14, 2024)

We investigate nonequilibrium excitations and charge transport in charge-neutral graphene driven with DC electric field by using the nonequilibrium Green's function technique. Due to the vanishing Fermi surface, electrons are subject to non-trivial nonequilibrium excitations such as highly anisotropic momentum distribution of electron-hole pairs, an analog of the Schwinger effect. We show that the electron-hole excitations, initiated by the Landau-Zener tunneling with a superlinear IV relation $I \propto E^{3/2}$, reaches a steady-state dominated by the dissipation due to optical phonons, resulting in a marginally sublinear IV with $I \propto E$, in agreement with recent experiments. The linear IV starts to show the sign of current saturation as the graphene is doped away from the Dirac point, and recovers the semi-classical relation for the saturated velocity. We give a detailed discussion on the nonequilibrium charge creation and the relation between the electron-phonon scattering rate and the electric field in the steady-state limit. We explain how the apparent Ohmic IV is recovered near the Dirac point. We propose a mechanism where the peculiar nonequilibrium electron-hole creation can be utilized in a novel infra-red device.

PACS numbers: 72.80.Vp, 73.50.Fq

I. INTRODUCTION

As a prototypical monolayer material, graphene has attracted much attention in the past decade for its extraordinary mechanical and electronic properties¹⁻³. The extraordinarily high mobility up to $10^5 \text{cm}^2/\text{Vs}$ and the current density up to 10^9A cm^{-2} in graphene⁴ make the system a prominent building element in nano-electronics. The peculiar linear dispersion relation of the band-structure at the charge-neutrality point has fascinated the physics community ever since the graphene could be mass-produced, due to its novel relativistic analog in a solid state system. The vanishing gap out of the honeycomb lattice has the most attractive aspects in the both worlds of semiconductor and metal: the maneuverability of the semiconductor and the cleanness of metal.

Among many fundamental questions unique to graphene, we explore here the role of the Dirac point in electronic transport. The DC transport experiments have shown the electric current in graphene tends to saturate under a high electric field of several tens of kV/cm ⁵⁻⁸. Theoretical and experimental studies have indicated that the tendency is due to the interaction between electrons and optical phonons^{5,6,9-12}. Despite the progress, the most theoretical studies have been limited to the Boltzmann transport theory and applied mostly to samples with high electron densities. We present a detailed study of electronic excitations and the transport close to the Dirac point by using the microscopic calculation based on the Keldysh Green's function method. We employ the formulation recently developed for the dissipative steady-state nonequilibrium under a DC electric field¹³, applicable for experimental DC transport measurements.

Recently, various transport mechanisms in graphene have been proposed. Boltzmann transport theory⁵ and a

streaming model¹² have been successful to describe the behavior of the velocity saturation in the limit of large current density. However, in the charge-neutrality limit, the peculiarity of the Dirac point demands proper quantum mechanical treatment of the nonequilibrium effects. It has been argued that the Landau-Zener tunneling¹⁴ should play an important role in the nonequilibrium state near the Dirac point¹⁵⁻²¹, where the electric field creates excitations in pairs of electron and hole, dramatically changing its equilibrium electronic properties. This effect can be considered a solid-state analog of the Schwinger effect²²⁻²⁵. However, the main consequence from the theory on the current-voltage relation, $I \sim V^\alpha$ with the exponent α greater than one, has been inconsistent with majority of the measured DC transport in graphene^{6,8,26} where the current saturation gradually crosses over to a linear or marginally sublinear $I - V$ relation ($\alpha \approx 1$).

To investigate the transport mechanism, we start from a conventional quantum mechanical tight-binding model for graphene lattice with coupling to on-site phonons to simulate the optical phonons. In addition, we implement the dissipation mechanism in the form of fermion baths^{27,28} to mimic the dissipation into an infinite medium which is essential to establish a rigorous steady-state nonequilibrium limit within the defined Hamiltonian. We use the Keldysh formalism¹³ to obtain the steady-state Green's function (GF) and then transport quantities. The calculation confirms the semi-classical behaviors away from the Dirac point, predicted by the Boltzmann transport theory. In the charge-neutrality limit, the excitation population is linearly proportional to the electric field in the presence of the coupling to optical phonons, while the drift velocity saturates to about 50% of the Fermi velocity⁸. Despite the reversed role of the charge excitation and the drift velocity in the Drude

metal, an apparent Ohmic relation $I \propto V$ is established. Furthermore, the electron-hole pair creation is strongly anisotropic occupying the same region of the momentum space in the upper and lower Dirac cones, which makes the system a strong candidate for an infra-red switching device.

The paper is organized as follows. In Section II, the model and the methodology are detailed. Especially, the construction of the lattice summation in the nonequilibrium Dyson equation is explained. In Section III, we first discuss the Landau-Zener effect in the absence of the optical phonons. We then discuss the effect of the phonons on IV -relation and the excitation distribution. We give detailed analysis and microscopic justification for the saturated transport limit through electron-phonon (el-ph) coupling. In Section IV, we summarize and speculate possible device application by exploiting the peculiar excitation spectrum in graphene.

II. FORMULATION

A. Model

We introduce a dissipative lattice model which consists of tight-binding Hamiltonian coupled to bath systems with open boundary. We solve the problem strictly within the given Hamiltonian according to the Keldysh formalism, and as established previously^{13,27-29}, the coupling to infinite degrees of freedom facilitates the infinite-time limit for steady-states under a DC electric field. We use fermion baths to mimic the continuous medium for Ohmic dissipation. In addition, we include the inelastic scattering mechanism provided by optical phonons which will be shown to be crucial to understand the transport phenomena in graphene.

The Hamiltonian is broken up as follows.

$$H = H_{\text{TB}} + H_{\text{bath}} + H_{\text{ph}} + H_{\text{E}}. \quad (1)$$

H_{TB} is the tight-binding model of graphene defined on a honeycomb lattice as shown in FIG. 1. H_{bath} is the coupling to fermion baths, and H_{ph} the coupling to optical phonons. H_{E} is the energy shift of the tight-binding and bath orbitals due to the external electric field E .

The tight-binding Hamiltonian H_{TB} is defined on a monolayer honeycomb lattice which is a system of interlaced triangular sublattices A and B as shown in FIG. 1. The Hamiltonian is written as

$$H_{\text{TB}} = -\gamma \sum_{\langle \mathbf{r}\mathbf{r}' \rangle} d_{\mathbf{r}}^{\dagger} d_{\mathbf{r}'}, \quad (2)$$

with the tight-binding parameter γ and the electron operator $d_{\mathbf{r}}$ defined on lattice vectors \mathbf{r} . The lattice summation is restricted to nearest neighbors, i.e., \mathbf{r} and \mathbf{r}' should be on different sublattices. The tight-binding parameter γ is typically 3 eV for graphene². We ignore the spin degree of freedom.

The coupling to the fermion reservoirs in the Hamiltonian, H_{bath} , is of the following form

$$H_{\text{bath}} = -\frac{g}{\sqrt{L}} \sum_{\mathbf{r}\alpha} (d_{\mathbf{r}}^{\dagger} c_{\mathbf{r}\alpha} + \text{H.c.}) + \sum_{\mathbf{r}\alpha} \epsilon_{\alpha} c_{\mathbf{r}\alpha}^{\dagger} c_{\mathbf{r}\alpha}. \quad (3)$$

Here, we attach a fermion continuum to each fermion site \mathbf{r} . $c_{\mathbf{r}\alpha}$ is the electron operator in the continuum at the \mathbf{r} site with the continuum index α at energy ϵ_{α} . For simplicity, we assume that the energy spectrum of ϵ_{α} has a constant density of states. Then the hybridization of the \mathbf{r} -site to the reservoir is given by the damping parameter Γ as $\Gamma = L^{-1} \pi g^2 \sum_{\alpha} \delta(\epsilon_{\alpha})$ with the volume normalization by L . This provides a physical mechanism to dissipate excess energy created by external fields and enables a steady state with a finite current. The scattering time due to acoustic phonons scales linearly^{30,31} with electron energy and is up to about 5 ps⁻¹ within the Dirac cone¹², which corresponds to $\Gamma/\gamma \sim 5 \times 10^{-4}$ in our model. We emphasize that the dissipation of the model is not inside the leads, as often considered in nano-junction models, but comes from the *bulk* dissipation where the energy relaxation occurs over the whole system.

Electrons in the monolayer lattice interact with both acoustic and optical phonons. The former has zero energy gap and can be excited by arbitrarily small energy. In the low-field regime, interaction with acoustic phonons provides a fundamental channel of electronic scattering and energy dissipation. On the other hand, the optical phonons have a large gap $\hbar\omega_{\text{ph}}$ and interact strongly with electrons only through higher-energy processes. It is argued that the dissipation by acoustic phonons is described by considering the exactly soluble fermion-reservoir model²⁷. In the regime of small dissipation, this model reproduces successfully the Boltzmann transport theory and gives the correct linear response behavior^{13,28}. This motivates us to consider the graphene lattice coupled to fermion reservoirs at each lattice site.

In the strong-field transport, inclusion of inelastic scattering becomes crucial and we consider the optical phonons at frequency $\omega_{\text{ph}} \approx 150$ meV ($\hbar = 1$ unit is used)¹¹. Each lattice site couples to an independent (optical) phonon bath with coupling constant g_{ep} . The el-ph coupling takes the typical Holstein model as

$$H_{\text{ph}} = g_{\text{ep}} \sum_{\mathbf{r}} (a_{\mathbf{r}} + a_{\mathbf{r}}^{\dagger}) d_{\mathbf{r}}^{\dagger} d_{\mathbf{r}} + \sum_{\mathbf{r}} \omega_{\text{ph}} a_{\mathbf{r}}^{\dagger} a_{\mathbf{r}}, \quad (4)$$

with $a_{\mathbf{r}}$ being the annihilation operator of optical phonons at position \mathbf{r} .

The last term in the Hamiltonian is the potential shift by the DC electric field. We choose the Coulomb gauge with the static potential $-\mathbf{r} \cdot \mathbf{E}$ ($e = 1$ unit is used).

$$H_{\text{E}} = -\sum_{\mathbf{r}} \mathbf{r} \cdot \mathbf{E} \left(d_{\mathbf{r}}^{\dagger} d_{\mathbf{r}} + \sum_{\alpha} c_{\mathbf{r}\alpha}^{\dagger} c_{\mathbf{r}\alpha} \right). \quad (5)$$

The summation is over the sites \mathbf{r} with infinite size lattice. We set the bath chemical potentials to match the

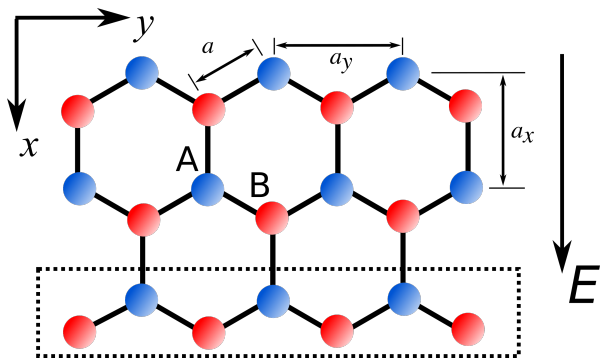


FIG. 1. Tight-binding model of graphene. The hexagonal lattice structure is composed of two triangular sublattices labeled as A (blue) and B (red). The dashed line encircles a “zig-zag” row perpendicular to the field-direction.

level shift by the electric field, i.e., $\mu_{\text{bath}}(\mathbf{r}) = -\mathbf{r} \cdot \mathbf{E}$ so that each sites are equivalent except for the relative energy shift. In the following discussions, unless specifically mentioned, we reserve the chemical potential notation μ to that in the zero field limit.

B. Recursion relations

To solve the model, we utilize the dynamical mean-field theory (DMFT)³² within the Keldysh GF formalism, and ignore the inter-site self-energy by the el-ph coupling. In addition to that we keep the nonequilibrium GFs, the main difference from the equilibrium DMFT is that the lattice summation in the DMFT cannot be performed by a sum over wavevectors due to the bias potential. Although the lattice summation is possible by a brute-force matrix inversion in real-space, a much more efficient algorithm can be used in the spatially uniform limit, as proposed in Ref. 13.

We note that the wavevector component p_y perpendicular to the field E is a good quantum number, and we organize the Hamiltonian as depicted in FIG. 1 into zig-zag rows (dashed rectangle, indexed by ℓ). We consider the hopping within the row parametrized by p_y , and then exactly treat the inter-row hopping through the self-energy addition $\mathbf{F}_{\pm}(\omega)$ from the (semi-infinite) upper rows and the lower rows, respectively.

To proceed, we diagonalize the Hamiltonian within the ℓ -th row with the Fourier transform $d_{\ell s}^{\dagger}(p_y) = \frac{1}{\sqrt{N_y}} \sum_{\mathbf{r} \in \{\ell s\}} e^{ip_y \mathbf{r} \cdot \hat{\mathbf{e}}_y} d_{\mathbf{r}}^{\dagger}$, where the summation is limited to all atoms inside the ℓ -th row and with the sublattice index $s = \pm$ (or A/B). N_y is the number of atoms in a row for normalization. We then obtain the transverse Hamiltonian per momentum p_y :

$$H_{\text{TB},\perp}(p_y) = -2\gamma \sum_{\ell} \cos(p_y a_y / 2) d_{\ell A}^{\dagger}(p_y) d_{\ell B}(p_y) + H.c. \quad (6)$$

The constant $a_y = \sqrt{3}a$ is shown in FIG. 1. The longitudinal Hamiltonian is

$$H_{\text{TB},\parallel}(p_y) = -\gamma \sum_{\ell} d_{\ell+1,A}^{\dagger}(p_y) d_{\ell B}(p_y) + H.c. \quad (7)$$

Now the problem is reduced to solving an effectively one-dimensional problem parametrized by p_y , where a central row ($\ell = 0$) is connected to two semi-infinite chains with upper ($\ell > 0$) and lower ($\ell < 0$) rows via $H_{\text{TB},\parallel}(p_y)$.

Given p_y , the GFs $\mathbf{G}^{\lessgtr}(\omega; p_y)$ at $\ell = 0$ are expressed in the 2×2 sublattice space. By denoting the GF on the edge row of the semi-infinite chains as $\mathbf{F}_{\pm}(\omega; p_y)$, we construct the (retarded) GF as

$$\mathbf{G}^r(\omega; p_y)^{-1} = \omega - \mathbf{h}_{\perp}(p_y) - \Sigma^r(\omega) - \sum_{\alpha=\pm} \mathbf{v}_{\alpha}^{\dagger} \mathbf{F}_{\alpha}^r(\omega + \alpha E a_x; p_y) \mathbf{v}_{\alpha}, \quad (8)$$

with a given local self-energy $\Sigma^r(\omega)$ and the intra-row Hamiltonian matrix from Eqs. (6) and (5)

$$\mathbf{h}_{\perp}(p_y) = \begin{pmatrix} 0 & -2\gamma \cos(p_y a_y / 2) \\ -2\gamma \cos(p_y a_y / 2) & -E a / 2 \end{pmatrix}. \quad (9)$$

The matrix \mathbf{v}_{\pm} is to connect the sublattices via hopping

$$\mathbf{v}_{+} = \mathbf{v}_{-}^{\dagger} = \begin{pmatrix} 0 & \gamma \\ 0 & 0 \end{pmatrix}. \quad (10)$$

The GF on the semi-infinite chains $\mathbf{F}_{\alpha}^{\lessgtr}(\omega; p_y)$ is calculated recursively¹³. By exploiting the self-similarity between the edge and the next-to-edge rows, we have the relation

$$\mathbf{F}_{\alpha}^r(\omega; p_y)^{-1} = \omega - \mathbf{h}_{\perp}(p_y) - \Sigma^r(\omega) - \mathbf{v}_{\alpha}^{\dagger} \mathbf{F}_{\alpha}^r(\omega + \alpha E a_x; p_y) \mathbf{v}_{\alpha}. \quad (11)$$

Similarly, the lesser GFs can be computed with the Dyson's equations¹³,

$$\begin{aligned} \mathbf{G}^{<}(\omega; p_y) &= \mathbf{G}^r(\omega; p_y) \left[\Sigma^{<}(\omega) \right. \\ &\quad \left. + \sum_{\alpha=\pm} \mathbf{v}_{\alpha}^{\dagger} \mathbf{F}_{\alpha}^{<}(\omega + \alpha E a_x; p_y) \mathbf{v}_{\alpha} \right] \mathbf{G}^a(\omega; p_y) \\ \mathbf{F}_{\alpha}^{<}(\omega; p_y) &= \mathbf{F}_{\alpha}^r(\omega; p_y) [\Sigma^{<}(\omega) \\ &\quad + \mathbf{v}_{\alpha}^{\dagger} \mathbf{F}_{\alpha}^{<}(\omega + \alpha E a_x; p_y) \mathbf{v}_{\alpha}] \mathbf{F}_{\alpha}^a(\omega; p_y). \end{aligned} \quad (12)$$

We complete the DMFT loop in the usual manner. The local GF is defined as $\mathbf{G}_{\text{loc}}(\omega) = \frac{1}{N_y} \sum_{p_y} \mathbf{G}(\omega; p_y)$. Once we have $\mathbf{G}_{\text{loc}}(\omega)$ and $\Sigma(\omega)$, we construct the (non-interacting) Weiss-field GF $\mathcal{G}(\omega)$ as

$$\mathcal{G}^r(\omega)^{-1} = \mathbf{G}_{\text{loc}}^r(\omega)^{-1} + \Sigma^r(\omega), \quad (13)$$

for the retarded functions. Then the Weiss-field $\mathcal{G}(\omega)$ is used to update the self-energy $\Sigma(\omega)$ which is then used to

update the GFs again, as described so far. The procedure is repeated until convergence.

The self-energy has the contribution from the fermion baths and the el-ph coupling: $\Sigma(\omega) = \Sigma_\Gamma(\omega) + \Sigma_{\text{ph}}(\omega)$. Within the DMFT, the self-energies are diagonal in the sublattice space. The self-energy by the fermion baths (at $\ell = 0$) is given as

$$\Sigma_\Gamma^r(\omega) = -i\Gamma, \Sigma_\Gamma^<(\omega) = -2i\Gamma \begin{pmatrix} f_0(\omega) & 0 \\ 0 & f_0(\omega + Ea/2) \end{pmatrix}, \quad (14)$$

with the Fermi-Dirac function at the bath temperature. The bath temperature has been chosen as $T_{\text{bath}} = 0.01\gamma \approx 350\text{K}$ unless stated otherwise. For the el-ph coupling, we use the approximation that the phonon GFs are not dressed with the self-energy

$$\Sigma_{\text{ph},ss}^<(\omega) = g_{\text{ep}}^2 [\mathcal{G}_{ss}^>(\omega - \omega_{\text{ph}})(N_{\text{ph}} + 1) + \mathcal{G}_{ss}^<(\omega + \omega_{\text{ph}})N_{\text{ph}}], \quad (15)$$

with $N_{\text{ph}} = 1/[\exp(\omega_{\text{ph}}/T_{\text{ph}}) - 1]$ the Bose-Einstein distribution and the phonon temperature T_{ph} . We assume that $\omega_{\text{ph}} \gg T_{\text{ph}}$ with $\omega_{\text{ph}} \sim 1500\text{K}$, and that the renormalization of the phonon is not strong.

This approximation is in line with the semiclassical pictures adopted in previous works^{5,6}. For very large electric fields, the physics may be affected by the hot (optical) phonons excited during the transport process. However, this effect is minimized if phonons are strongly coupled with the environmental bath, and lose energy immediately. In Section III. E, we estimate the hot-electron temperature T_{eff} for a charge-neutral graphene in the range of $\sim 500\text{K}$, and we expect the phonon temperature T_{ph} to be significantly lower than T_{eff} and ω_{ph} .

III. RESULTS

A. Signature of Landau-Zener tunneling

We first consider the strong-field transport in graphene without optical phonon interaction. The transport behavior is quite different between the cases with zero and finite chemical potential μ . With $\mu > 0$, a non-zero Fermi circle exists in the upper band, allowing the semiclassical Boltzmann transport theory to be applied: electric fields displace the Fermi circle in the field direction, as shown in the FIG. 2(a). With a scattering-time τ , the Fermi circle is displaced by $E\tau$. Similar argument can be made for holes in the case of $\mu < 0$. With $\mu = 0$ the Fermi circle shrinks to a point, as in FIG. 2(b), and the conventional linear response theory does not apply. Near this point, an electric field excites electrons to the upper band, leaving holes in the lower band. These nonequilibrium excitations are initially driven by the Landau-Zener transition, and the electrons are accelerated by the electric field during the scattering time τ , resulting in a highly anisotropic excitation distribution. The excitation distribution in the momentum space forms streaking lines

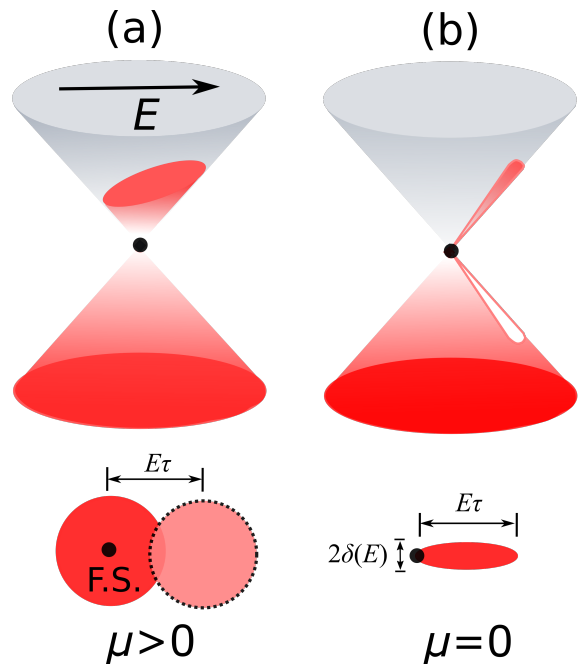


FIG. 2. Schematic demonstration of momentum distribution of electric-field-driven graphene (a) off the Dirac point and (b) on the Dirac point. (a) Chemical potential $\mu > 0$ and a finite Fermi sphere exists in equilibrium. An electric field displaces the Fermi sphere by $E\tau$ according to the semiclassical picture. (b) $\mu = 0$ and the “Fermi sphere” becomes point-like. In this case, any finite field transport effect is of quantum mechanical nature and should be related to creation of particle-hole pairs. A jet-like distribution for both electrons and holes is created under a finite electric field in the charge-neutral limit.

in the particle and hole cones along the direction of the field. This is a solid-state analog of the Schwinger effect²², a particle-antiparticle pair creation by an intense electric field with zero mass gap.

With an electric field in the x -direction, the perpendicular momentum p_y is a good quantum number and we analyze the excitations on the dispersion relation on a sliced cone at a fixed p_y , as shown in FIG. 3. At $p_y \neq 0$, the dispersion relation is gapped with the charge gap $2\Delta = 2v_F|p_y|$. The transition of an electron from the lower band to the upper band due to a constant force field is described by the Landau-Zener tunneling with the transition probability γ_{LZ} as

$$\gamma_{\text{LZ}} = \exp(-\pi\Delta^2/v_F E) = \exp(-\pi v_F p_y^2/E). \quad (16)$$

This suggests that electrons only with $|p_y| \lesssim \sqrt{E/\pi v_F} \equiv \delta_0(E)$ are excited to the upper band (with the subscript 0 referring to without phonons). On the other hand, the range of excitation of the longitudinal momentum p_x is given by the lifetime of the excited electrons. The fermion bath provides the lifetime^{27,33} $\tau_\Gamma = (2\Gamma)^{-1}$ and the range of p_x for excited electrons become $0 \lesssim p_x \lesssim E\tau_\Gamma$. Combining these observations, an Ansatz is proposed for the

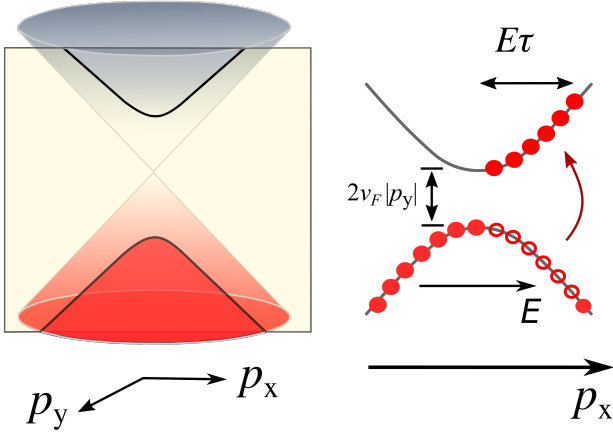


FIG. 3. Demonstration of Landau-Zener tunneling in graphene on the Dirac point. When the Dirac cone intersects with a plane of non-zero p_y , the excitations in the gapped quasi-1D dispersion relation is understood in terms of the Landau-Zener tunneling. Significant electron-hole pairs are created for $|p_y| \lesssim \delta(E)$.

momentum distribution for the excitations as

$$n_{\mathbf{p}} \propto \theta(\delta_0(E) - |p_y|)\theta(E\tau_{\Gamma} - p_x)\theta(p_x), \quad (17)$$

and the number of excited electrons n_{ex} behaves as

$$n_{\text{ex}} \propto \delta_0(E) \cdot E\tau_{\Gamma} \propto E^{3/2}/\Gamma. \quad (18)$$

The excitation of holes has the exact same distribution as the electrons, with the jet-like excitation on the same side of the momentum. Similar momentum distribution has been proposed in the streaming model¹², where the Fermi sea is elongated in the direction of the field by $E\tau$. However, in the $\mu = 0$ limit, a finite Fermi sea does not exist and this phenomenological approach does not provide any mechanism for the width of the stream.

In the limit of $E\tau_{\Gamma} \gg \delta_0(E)$, the jet-like distribution is almost completely aligned with the electric field and the averaged velocity is close to v_F , resulting in $J \propto n_{\text{neq}}v_F \propto E^{1.5}\tau_{\Gamma}$, which is verified in FIG. 4. In the absence of the el-ph coupling ($g_{\text{ep}} = 0$), the $J \propto E^{1.5}$ scaling law is shown (solid lines) with the power greater than one as the signature of Landau-Zener mechanism. The inset shows the collapse of data to the form $J \sim E^{1.5}/\Gamma$.

When the optical phonon interaction is turned on ($g_{\text{ep}} \neq 0$), the superlinear JE relation becomes marginally sublinear. The strongly inelastic scattering by optical phonons reduces the current, as shown in FIG. 4(a). It is interesting that the window for the $J \sim E^{3/2}$ shrinks as the damping Γ is reduced, whereas it may be naively expected that a clean limit ($\Gamma \rightarrow 0$) may preserve the peculiar fractional power law. This can be explained as follows. In the small Γ limit, the electrons lifetime increases and the energy increase due to the acceleration $v_F \cdot (E\tau_{\Gamma})$ reaches the optical phonon threshold $\hbar\omega_{\text{ph}}$ at a smaller field E . This is consistent with

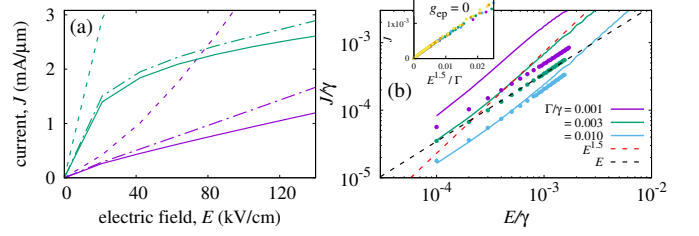


FIG. 4. $J - E$ relation of graphene under strong field. (a) Deviations of current from non-interacting case ($g_{\text{ep}} = 0.0$, dash lines) to $g_{\text{ep}}^2/\omega_{\text{ph}} = 4\gamma$ (dotted dash lines) and 8γ (solid lines). The damping $\Gamma = 0.001\gamma$. The blue (purple) lines are with $\mu = 0.10\gamma$ ($\mu = 0.0\gamma$). (b) The currents with (dots) and without (solid lines) the optical-phonon interactions at different damping parameter Γ . As damping increases, the range of electric field in which $J \propto E^{1.5}$ holds expands. The inset shows the current as a function of $E^{1.5}/\Gamma$ for a variety of $\Gamma = 0.001, 0.003, 0.005, 0.007, 0.100$. In (b), $g_{\text{ep}}^2/\omega_{\text{ph}} = 4\gamma$ for dots. Optical phonon frequency ω_{ph} is 0.05γ . In all plots in this paper, γ is set to 3 eV.

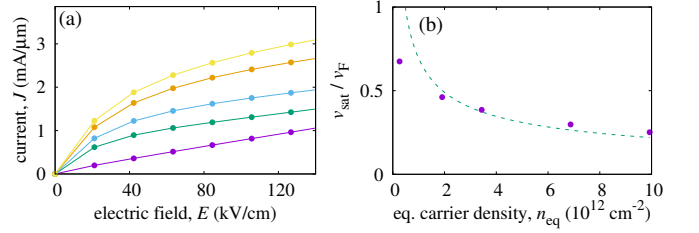


FIG. 5. (a) $J - E$ curve for different chemical potential μ . As system is taken away from the Dirac point, current increases and shows the saturating behaviour under high-field. The $J - E$ curves in (a) have chemical potentials $\mu = 0.0, 0.05, 0.07, 0.10, 0.12$ from bottom to top. (b) Computed relation (dots) $v_{\text{sat}} \propto 1/\sqrt{n_{\text{eq}}}$ between the saturated velocity v_{sat} and the equilibrium charge density n_{eq} . This is consistent with the semiclassical formula (19) (dashed line). $\Gamma = 0.003\gamma$, $\omega_{\text{ph}} = 0.05\gamma$ and $g_{\text{ep}}^2/\omega_{\text{ph}} = 8\gamma$.

the findings that the superlinear behavior is observed in low-mobility devices under DC-electric field²⁰, as well as graphene samples excited by THz electric pulses¹⁸. In the clean limit, the observed JE relations remain close to linear in strong-field transport experiments^{6,26}.

B. Steady-state current at large fields

Now we study the effect of optical phonon interaction more closely. Recently, the phenomena of current saturation have attracted intense interest.^{7,8,10,11,34} It is found that the current saturation in graphene at high electric field depends on the optical phonon frequency ω_{ph} and equilibrium current carrier density n_{eq} . The former is a parameter independent of electric control, and the latter is controlled through the chemical potential μ . We are mostly interested in how the graphene behaves under dif-

ferent chemical potentials, especially when it is close to the Dirac point $\mu = 0$. FIG. 5 systematically shows calculated $J \sim E$ relations with a set of realistic parameters. In graphene, the tight-binding hopping parameter $\gamma \approx 3$ eV and the optical phonon frequency $\omega_{\text{ph}} = 0.05\gamma \approx 150$ meV. These values are close to the empirical parameter used in previous works^{8,11,12}.

In FIG. 5, the electronic current generally shows the tendency to saturate under high electric fields in the samples with relatively high equilibrium electron density. Previous semi-classical analyses^{5,12} have assumed that Fermi sphere is shifted by $\hbar\omega_{\text{ph}}/v_F$, leading to an empirical formula of the saturated velocity,

$$v_{\text{sat}} = \frac{1}{\sqrt{\pi}} \frac{\omega_{\text{ph}}}{\sqrt{n_{\text{eq}}}}, \quad (19)$$

where n_{eq} is the equilibrium current carrier density. While this expression has been confirmed experimentally, the formula obviously breaks down when ω_{ph} is too large or n_{eq} is too small, since v_{sat} can never be greater than v_F . Our main interest is in the regime the approximation fails. Our calculations do not show true saturation of current and we derive the drift velocity according to a phenomenological model¹¹:

$$v_d = \frac{\chi_0 E}{1 + \chi_0 E/v_{\text{sat}}}, \quad (20)$$

where χ_0 is the zero-field mobility. As verified in FIG. 5(b), the extracted v_{sat} follows $1/\sqrt{n_{\text{eq}}}$ relation until the Dirac point is reached. Interestingly, recent measurements using short bias pulses⁸ reported similar range of the maximum drift velocity $v_d \approx 0.5 \times v_F$ close to the Dirac point.

C. Evolution of momentum distribution under external field

To further understand the steady-state current due to the optical phonon scattering, we look at the evolution of momentum distribution $n_{\mathbf{p}}$ under electric fields. At $\mu > 0$ a finite Fermi sea exists around the center of the Dirac cone, as shown in FIG. 6 for the current and momentum distributions. The Fermi sea is shifted along the field-direction when electric field is applied. However, at high electric fields, the Fermi sea stops to shift due to the strong relaxation by the optical phonons when electrons lose their excess energy to phonon baths. This is consistent with the semi-classical Boltzmann transport calculations.⁹

At $\mu = 0$, as shown in FIG. 7(a), the current increases almost linearly without saturation. To investigate the origin, we plot the electron excitation n_{ex} and the drift velocity v_d calculated by

$$v_d = v_F \frac{\int_{|\mathbf{p}| < \Lambda_p} n(\mathbf{p}) \cos \theta d^2 \mathbf{p}}{\int_{|\mathbf{p}| < \Lambda_p} n(\mathbf{p}) d^2 \mathbf{p}}, \quad (21)$$

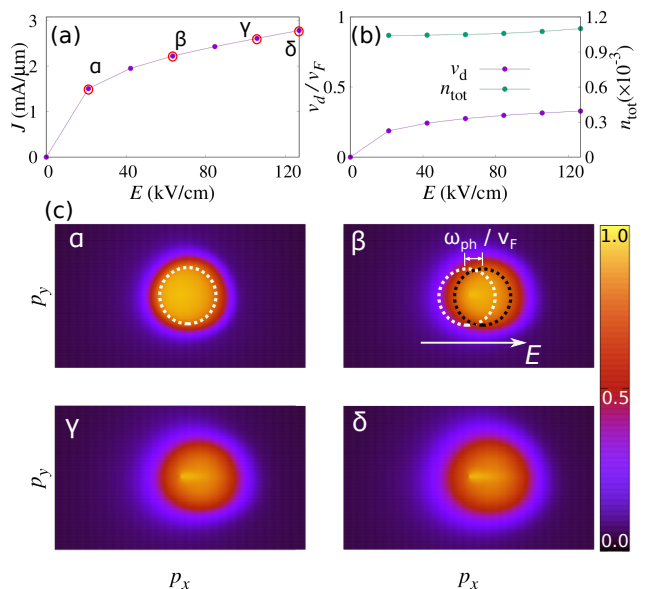


FIG. 6. Charge excitations and the momentum distribution of electrons under electric fields in the off-Dirac-point graphene. (a) Saturation of current under electric fields and (b) drift velocity v_d and total current carriers number n_{tot} under electric fields. The v_d saturates like current, and n_{tot} is almost unchanged. (c) Momentum distributions of electrons at $\mu = 0.1\gamma$. Fermi sea is shifted at small electric fields. Its displacement is nearly unchanged at high fields. Near $\mathbf{p} = 0$, a faint signature of the Schwinger effect can be seen in the panels γ and δ .

with the angle θ between the field and momentum vectors, and the large momentum cutoff Λ_p . It is clear that the drift velocity saturates at small field and the main contribution to the current $J = n_{\text{ex}} v_d$ is due to the electron excitations linearly proportional to the field E . We emphasize that the drift velocity is evaluated by dividing the current by the excited charge out of neutrality, instead of the equilibrium charge n_{eq} as often used in experimental estimates.

Let us investigate more into the excitations in the momentum space. FIG. 7(c) shares the characteristics proposed in Eq. (17). However, coupling to the inelastic phonons results in important differences. First, as the electric field increases, the length of the jet stops growing but saturates to the length related to the phonon frequency, $(p_x)_{\text{max}} \sim 2\omega_{\text{ph}}/v_F$ with the center of distribution at ω_{ph}/v_F . Therefore, $E\tau_T$ in Eq. (17) is replaced by $2\omega_{\text{ph}}/v_F$. Second, the width of the distribution $\delta(E)$ no longer follows the Landau-Zener form $\delta_0(E) \propto \sqrt{E}$. As the distribution saturates, the width $\delta(E)$ gets smeared due to the local scattering by optical phonons, which can be summarized as

$$n_{\mathbf{p}} \propto \theta(\delta(E) - |p_y|) \theta(2\omega_{\text{ph}}/v_F - p_x) \theta(p_x). \quad (22)$$

Due to the smearing of the momentum distribution with stronger el-ph scattering at high fields, the drift velocity

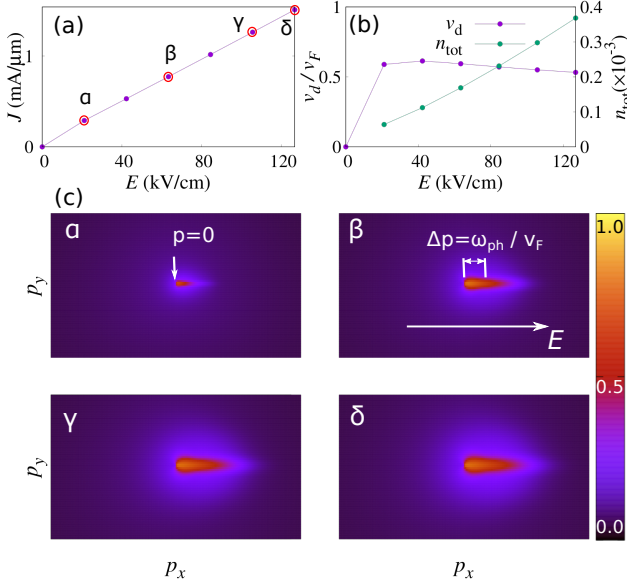


FIG. 7. Charge excitations and the momentum distribution of electrons under electric fields in the on-Dirac-point graphene. (a) Current which scales linearly with electric field. (b) Drift velocity v_d and total number of current carriers n_{tot} . The drift velocity overshoots and then decreases due to optical phonon emission. And the total number of excitations n_{tot} increases monotonically with E . (c) Momentum distribution of electrons (upper band). At high fields, the center of excitation distribution is at the momentum $p_x = \Delta p \approx \omega_{\text{ph}}/v_F$. The distribution of holes is essentially identical.

is slightly reduced with a wider angular distribution in Eq. (21), as shown in FIG. 7(b).

D. Energy dissipation

To understand the strong-field IV -relation at Dirac point with optical-phonon interaction, we look into the energy conservation law: the electric power JE is equal to the dissipation rate. In the case when the optical phonon scattering dominates at large E , the scattering rate is $\tau_{\text{ph}}^{-1} = -\text{Im}(\Sigma_{\text{ph}}^< - \Sigma_{\text{ph}}^>)$ and each scattering between an electron and optical phonon reduces the electron energy by $\hbar\omega_{\text{ph}}$. So the dissipation rate of nonequilibrium excitations is $n_{\text{ex}}\omega_{\text{ph}}\tau_{\text{ph}}^{-1}$. The system at finite temperature can have a small equilibrium current carrier density n_{eq} , but we will concentrate on the $\mu = 0$ case where $n_{\text{eq}} \approx 0$, and the total electron density $n_{\text{tot}} \approx n_{\text{ex}}$. We then have

$$JE = n_{\text{ex}}\omega_{\text{ph}}\tau_{\text{ph}}^{-1} + \Theta_{\Gamma}. \quad (23)$$

The Θ_{Γ} is the dissipation rate due to fermion reservoirs. In the following, we will focus on the case where Θ_{Γ} is physically negligible. This approximation is tested in FIG. 8(a), with τ_{ph} being the scattering rate at $\omega = 0$.

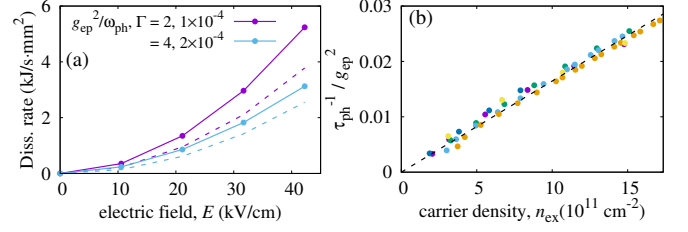


FIG. 8. (a) Energy dissipation rate in the presence of optical phonons with frequency ω_{ph} , and (b) the observed $\tau_{\text{ph}}^{-1} \propto n_{\text{ex}}$ relation. In (a), the dots are total dissipation rate JE , and the dashed lines are the dissipation rates due to optical phonon emission, predicted by Eq. (23). The predicted dissipation rate does not deviate much from the numerically calculated values at strong optical phonon interaction. We have assumed $\hbar\omega_{\text{ph}} \approx 150$ meV and $\Gamma \sim 0.0001\gamma$, which corresponds to $\tau_{\Gamma}^{-1} \sim 1$ ps $^{-1}$ assuming $\gamma = 3$ eV. The $g_{\text{ep}}^2/\omega_{\text{ph}} \sim 2\gamma$ leads to τ_{ph}^{-1} being in the order of 10 ps $^{-1}$. In (b), the linear relation of $\tau_{\text{ph}}^{-1} = \alpha n_{\text{ex}}$ is tested for a variety of interaction strengths $g_{\text{ep}}^2/\omega_{\text{ph}} = 2, 4, 8, 12, 16$ and $\Gamma = 0.0001, 0.0002, 0.001$.

The el-ph scattering rate τ_{ph}^{-1} is given as a convolution of electron and phonon Green's functions and is thus proportional to the electron density. We show that

$$\tau_{\text{ph}}^{-1} = \alpha n_{\text{ex}}, \quad (24)$$

as in FIG. 8(b), with the coefficient α explicitly calculated in Appendix B. It is shown both theoretically and numerically that α is proportional to g_{ep}^2 , given by $\alpha = \pi A_c g_{\text{ep}}^2 / 2\omega_{\text{ph}}$. The parameter α is independent of the electric field, and it can be evaluated experimentally at zero field by the line broadening of the electrons due to phonons.

A crucial step to understand the linear $J-E$ relation is the relation $n_{\text{ex}} \propto E$. We may relate the el-ph scattering rate τ_{ph}^{-1} in two different ways. One can argue that, in the high-field limit, the frequency of the el-ph scattering is determined by how fast the electron energy gained by the E -field reaches the optical phonon frequency, that is, with the average energy excitation at momentum Δp [see FIG. 7(c)] given as $v_F \Delta p = v_F E \tau_{\text{ph}} \sim \omega_{\text{ph}}$, which leads to $\tau_{\text{ph}}^{-1} \sim v_F E / \omega_{\text{ph}}$. This result is consistent with a more careful analysis based on Eq. (23). In the saturated drift velocity limit, the current J in the energy-conservation relation (23) is replaced by $n_{\text{ex}} v_{\text{sat}}$. We then obtain

$$\tau_{\text{ph}}^{-1} = v_{\text{sat}} E / \omega_{\text{ph}}. \quad (25)$$

after eliminating n_{ex} .

By eliminating τ_{ph}^{-1} from the Eqs. (24) and (25), we obtain

$$n_{\text{ex}} = \frac{v_{\text{sat}}}{\alpha \omega_{\text{ph}}} E, \quad (26)$$

and the current-field relation immediately follows close to the Dirac point (after restoring the physical constants)

$$J \approx n_{\text{ex}} v_{\text{sat}} = \frac{e^2 v_{\text{sat}}^2}{\alpha \hbar \omega_{\text{ph}}} E. \quad (27)$$

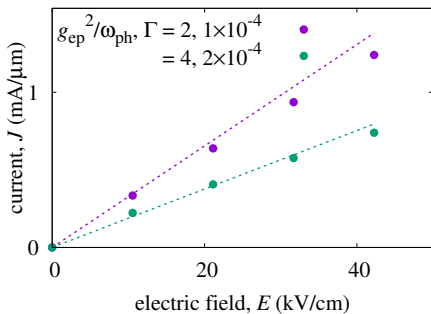


FIG. 9. $J - E$ relation of Dirac electron compared with the theoretical prediction. The theoretical $J - E$ relation (27) is compared against the numerical data (dots). $v_{\text{sat}} \sim 0.5v_F$ in the formula is extracted from the numerical data. The theory correctly predicts that the power of $J - E$ relation is close to one, and quantitatively matches the numerical data. Bath temperature is set to 35K in this calculation.

The saturated velocity has weak dependence on the electric field in the strong field limit. This result shows that the main electric field dependence originates from the charge excitation proportional to E . The formula is tested with numerical results in FIG. 9. The parameter v_{sat} is extracted from numerical calculations. In experiments, the formula may provide a way to extract v_{sat} from measured $I - E$ relation in the presence of both optical phonon emission and Landau-Zener tunneling. Using the relation $n_{\text{ex}}\tau_{\text{ph}} = \alpha^{-1}$, the $J - E$ relation can be cast in the usual Drude form as $J = (n_{\text{ex}}\tau_{\text{ph}}/m^*)E$ with the effective mass $m^{*-1} \sim v_{\text{sat}}^2/\hbar\omega_{\text{ph}}$ for the driven Dirac particles, whose kinetic energies are of the magnitude of $\hbar\omega_{\text{ph}}$.

We reemphasize that, despite its similarity to the Ohmic law of simple metals, the origin of the above linear $J - E$ relation is very different. In a simple metal, while the carrier density n_{eq} is weakly perturbed by the electric fields, the drift velocity v_d is proportional to the E -field. For the Dirac electrons in graphene, however, the role of the electric field is reversed: $v_d \approx v_{\text{sat}} \sim v_F$ at saturation while the nonequilibrium carriers density $n_{\text{ex}} \propto E$.

E. Effective temperature

A nonequilibrium effective temperature in a DC-transport system is the direct consequence of the balance between the electric power and the energy dissipation. Here, we follow the procedure in Ref. 29 to define the effective temperature from the nonequilibrium distribution function

$$f_{\text{loc}}(\omega) = -\frac{\text{Im}G_{\text{loc}}^<(\omega)}{2\text{Im}G_{\text{loc}}^r(\omega)}. \quad (28)$$

The nonequilibrium distribution function usually has a different functional form from the equilibrium Fermi-

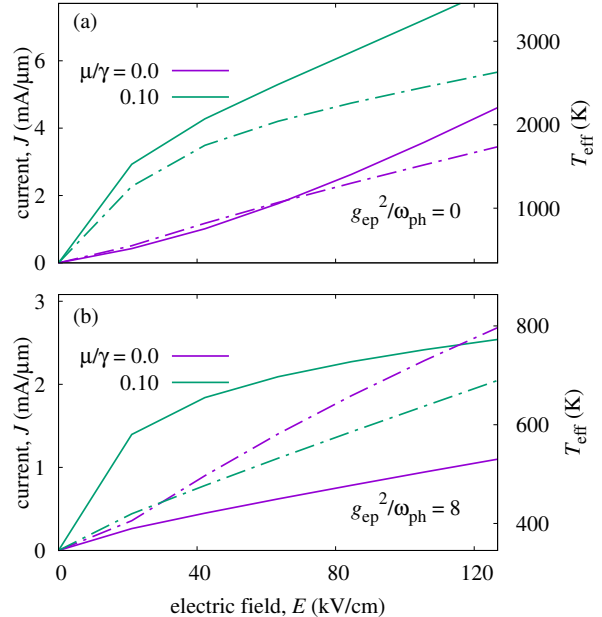


FIG. 10. Current and effective temperature of graphene (a) on and (b) off Dirac point. $\Gamma = 0.001\gamma$. The solid lines are currents, while dot-dashed lines are *nonequilibrium* effective temperature calculated under different electric fields. When optical-phonon coupling is switched off, the sample with $\mu = 0.10t$ (away from the Dirac point) shows higher effective temperature due to higher current as well as Joule heating; However, optical phonon emission results in current saturation as discussed above, and the behavior of T_{eff} becomes more complicated, with a crossover of T_{eff} occurring at finite electric fields.

Dirac distribution in which temperature is a well-defined parameter. To obtain a comparable nonequilibrium temperature parameter, we define the effective T_{eff} from the first moment of the distribution function,

$$\frac{\pi^2}{6}T_{\text{eff}}^2 = \int \omega [f_{\text{loc}}(\omega) - \theta(-\omega + \mu)] d\omega. \quad (29)$$

This definition is consistent with the Fermi-Dirac distribution at an equilibrium temperature.

With this definition, we plot the effective temperature in FIG. 10. In the case of $g_{\text{ep}} = 0$, effective temperature of the off-Dirac-point graphene is always higher than that of the on-Dirac-point system. This is because higher current carrier density results in higher current. The system with more current-carrying excitations create more Joule heating thereby the temperature is also higher. However, this is dramatically changed when optical phonon interaction is considered. In this case, the system with higher electron density still has higher electric current for all electric fields. However, at higher electric fields, the effective temperature of the off-Dirac-point system falls below the temperature of the Dirac-electron system.

To explain this crossover behavior, we note that the

effective temperature is the measure of the amount of excitations. As the electric field increases, the el-ph coupling overrides the relaxation by the fermion baths. As we argued above, the energy relaxation by phonons is proportional to the electronic charge density, and at non-zero μ , the finite Fermi surface makes the relaxation more efficient, thereby cools the electron temperature more effectively than at the $\mu = 0$ limit. The effective temperature is predicted to be in the range of 400-800 K in the realistic range of the electric field.³⁵⁻³⁹ We note that recent works^{40,41} have reported much higher hot-electron temperatures in graphene systems.

IV. CONCLUSION

We have demonstrated that Dirac electrons in graphene become excited in a non-trivial manner and lead to a marginally linear dependence of electric current under a DC electric field, through microscopic calculations based on the Keldysh Green's function theory. Inelastic scattering by optical phonons is shown to be crucial to produce the nonequilibrium charge excitation population n_{ex} and the electric current linearly proportional to the external field, close to a Dirac point, as summarized as

$$J \approx \frac{e^2 v_{\text{sat}}^2}{\alpha \hbar \omega_{\text{ph}}} E, \quad (30)$$

with the saturated drift velocity v_{sat} , the optical phonon frequency ω_{ph} , and the coefficient α proportional to the el-ph coupling constant. This proves mainly responsible for the apparent Ohmic relation although the mechanism is quite distinct from the Drude metal. This linear JE relation without saturation close to the Dirac point has been observed in clean graphene encapsulated by the hexa-boron-nitrides^{26,42}. Away from the Dirac charge-neutrality point, the conventional Boltzmann transport is recovered with the tendency for the current saturation with where the drift velocity is proportional to $\omega_{\text{ph}}/n_{\text{eq}}^{1/2}$ with the equilibrium charge density n_{eq} .

The electron-hole excitations at the charge-neutral point ($\mu = 0$) are strongly anisotropic in the momentum space with the excited electrons and holes flying in the same direction, an analog of the Schwinger effect in a solid state system. The inter-band creation of electron-hole pairs poses possibilities for optical applications. The continuous excitation energy up to the optical phonon energy of ~ 150 meV can be used for infra-red optical devices, without any lower threshold. Most intriguing is the change of the coupling of the electron-hole pairs to photons upon switching of the bias. Close to the Dirac point, the wavefunction under DC electric field acquires extra phase oscillation due to the potential gradient which can strongly suppress the photon-generation. When the electric-field is turned off, the electron wavefunction becomes a plane-wave and the coupling to the photon field enhances roughly by the factor proportional

to the length of the sample. This mechanism may be utilized in a fast-switching IR-optic diode.

V. ACKNOWLEDGEMENT

JL acknowledges the computational support from the CCR at University at Buffalo. We thank Jonathan P. Bird, Alexander Khaetskii and Huamin Li for their helpful discussions throughout the study.

Appendix A: Momentum distribution of electrons

To compute the momentum distribution of electrons, we note that $\mathbf{n}_{\mathbf{p}} = -i\mathbf{G}_{\mathbf{p}}^<(t, t) = -i\sum_{\mathbf{r}} \exp(i\mathbf{p} \cdot \mathbf{r})\mathbf{G}_{\mathbf{r}\mathbf{0}}^<(t, t)$. We have used matrix-valued Green's functions and $\mathbf{n}_{\mathbf{p},ss'} = -i\mathbf{G}_{\mathbf{p},ss'}^<(t, t)$. Using the time-translational invariance of the Green's functions, time t can be fixed as 0, so the momentum distribution is calculated as

$$\begin{aligned} \mathbf{n}_{\mathbf{p}} &= -i\sum_{\mathbf{r}} \exp(i\mathbf{p} \cdot \mathbf{r}) \int \frac{d\omega}{2\pi} \mathbf{G}_{\mathbf{r}\mathbf{0}}^<(\omega) \\ &= -i\sum_{\mathbf{r}} \exp(i\mathbf{p} \cdot \mathbf{r}) \int \frac{d\omega}{2\pi} \sum_{\mathbf{r}'} \mathbf{G}_{\mathbf{r}\mathbf{r}'}^r(\omega) \mathbf{\Sigma}^<(\omega + \mathbf{r}' \cdot \mathbf{E}) \\ &\quad \times \mathbf{G}_{\mathbf{r}'\mathbf{0}}^a(\omega), \end{aligned} \quad (A1)$$

where $\mathbf{\Sigma}^<(\omega) = \mathbf{\Sigma}_{\Gamma}^<(\omega) + \mathbf{\Sigma}_{\text{ph}}^<(\omega)$ is the total lesser self energy, including components from both fermion reservoirs and optical phonon baths. Now we shift $\omega \rightarrow \omega - \mathbf{r}' \cdot \mathbf{E}$, and notice that $\mathbf{G}_{\mathbf{r}+\mathbf{a}\mathbf{r}'+\mathbf{a}}^r(\omega) = \mathbf{G}_{\mathbf{r}\mathbf{r}'}^r(\omega + \mathbf{a} \cdot \mathbf{E})$, with \mathbf{r}, \mathbf{r}' and \mathbf{a} being lattice vectors. Therefore the formula is reduced to

$$\begin{aligned} \mathbf{n}_{\mathbf{p}} &= -\frac{i}{2\pi} \int d\omega \sum_{\mathbf{r}\mathbf{r}'} \exp(i\mathbf{p} \cdot \mathbf{r}) \mathbf{G}_{\mathbf{r}\mathbf{r}'}^r(\omega - \mathbf{r}' \cdot \mathbf{E}) \mathbf{\Sigma}^<(\omega) \\ &\quad \times \mathbf{G}_{\mathbf{r}'\mathbf{0}}^a(\omega - \mathbf{r}' \cdot \mathbf{E}) \\ &= -\frac{i}{2\pi} \int d\omega \sum_{\mathbf{r}\mathbf{r}'} \exp(i\mathbf{p} \cdot (\mathbf{r} - \mathbf{r}')) \mathbf{G}_{\mathbf{r}-\mathbf{r}',\mathbf{0}}^r(\omega) \mathbf{\Sigma}^<(\omega) \\ &\quad \times [\exp(-i\mathbf{p} \cdot \mathbf{r}') \mathbf{G}_{-\mathbf{r}'\mathbf{0}}^r(\omega)]^\dagger \\ &= -\frac{i}{2\pi} \int d\omega \mathbf{G}_{\mathbf{p}}^r(\omega) \mathbf{\Sigma}^<(\omega) \mathbf{G}_{\mathbf{p}}^a(\omega), \end{aligned} \quad (A2)$$

where we have defined $\mathbf{G}_{\mathbf{p}}^r(\omega) = \sum_{\mathbf{r}} \exp(i\mathbf{p} \cdot \mathbf{r}) \mathbf{G}_{\mathbf{r}\mathbf{0}}^r(\omega)$. In practical calculations, we firstly compute $\mathbf{G}_{\mathbf{r}\mathbf{0}}^r(\omega)$ and Fourier transform them to $\mathbf{G}_{\mathbf{p}}^r(\omega)$ in momentum space. Then $\mathbf{n}_{\mathbf{p}}$ is calculated by evaluating the integral in (A2). Finally, to interpret the result $\mathbf{n}_{\mathbf{p}}$, we should expand it in terms of equilibrium diagonalized basis²,

$$\begin{aligned} \psi_{\pm, \mathbf{p}} &= \frac{1}{\sqrt{2}} \begin{pmatrix} e^{-i\theta_{\mathbf{p}}/2} \\ \pm e^{i\theta_{\mathbf{p}}/2} \end{pmatrix}, \\ &\text{with } \theta_{\mathbf{p}} = \Delta_{\mathbf{p}}/|\Delta_{\mathbf{p}}|, \end{aligned} \quad (A3)$$

with $\Delta_{\mathbf{p}}$ given by

$$\Delta_{\mathbf{p}} = -\gamma \left(1 + 2e^{-ip_x a_x} \cos \frac{p_y a_y}{2} \right). \quad (\text{A4})$$

We define unitary transformation $U_{\mathbf{p}} = (\psi_{+,\mathbf{p}} \ \psi_{-,\mathbf{p}})$, and transform the $\mathbf{n}_{\mathbf{p}}$,

$$\tilde{\mathbf{n}}_{\mathbf{p}} = U_{\mathbf{p}}^\dagger \mathbf{n}_{\mathbf{p}} U_{\mathbf{p}} \quad (\text{A5})$$

Then the particle numbers for upper/lower bands are $\tilde{\mathbf{n}}_{\mathbf{p},++}$ and $\tilde{\mathbf{n}}_{\mathbf{p},--}$. These equations will be useful to calculate the nonequilibrium momentum distribution.

Appendix B: Derivation of Eq. (24), $\tau_{\text{ph}}^{-1} = \alpha n_{\text{ex}}$

In our self-consistent calculations, the 2nd-order electron self-energy by the optical phonon interaction is given by

$$\Sigma_{\text{ph}}^{\lessgtr}(\omega) \approx g_{\text{ep}}^2 G^{\lessgtr}(\omega \mp \omega_{\text{ph}}), \quad (\text{B1})$$

with coupling constant g_{ep} . The approximation is made due to the nearly empty optical phonon bath, where phonons are rarely excited before the nonequilibrium excitations having energy close to the optical phonon en-

ergy. Then the scattering rate at $\omega = 0$ becomes

$$\begin{aligned} \tau_{\text{ph}}^{-1} &= -ig_{\text{ep}}^2 [G^<(\omega_{\text{ph}}) - G^>(-\omega_{\text{ph}})] \\ &= 2\pi g_{\text{ep}}^2 [A(\omega_{\text{ph}})f_{\text{loc}}(\omega_{\text{ph}}) + A(-\omega_{\text{ph}})(1 - f(-\omega_{\text{ph}}))] \\ &= 4\pi g_{\text{ep}}^2 \rho(\omega_{\text{ph}}), \end{aligned} \quad (\text{B2})$$

with the particle-hole symmetry in the spectral function $A(\omega) = A(-\omega)$ and the distribution function $f_{\text{loc}}(\omega) = 1 - f_{\text{loc}}(-\omega)$ at the charge-neutrality point $\mu = 0$. $\rho(\omega) = A(\omega)f_{\text{loc}}(\omega)$ is the occupation density of electrons at frequency ω . As a first-order approximation, we again assume the jet-like distribution $n_{\mathbf{p}}$ is uniform within a thin rectangular box aligned in the field-direction and zero outside the box, as in Eq. (22). Note the number of excited electrons in the energy interval $[\omega, \omega + d\omega]$ should be

$$\rho(\omega)d\omega \propto \int_{\omega < v_F p < \omega + d\omega} n_{\mathbf{p}} d^2 \mathbf{p}. \quad (\text{B3})$$

This rectangle-shaped momentum distribution results in the uniform $\rho(\omega) \approx \rho(\omega_{\text{ph}})$ when $|\omega| \lesssim 2\omega_{\text{ph}}$ and zero otherwise. Then we have

$$n_{\text{ex}} = 2 \int d\omega \rho(\omega)/A_c \approx 4g_v \rho(\omega_{\text{ph}}) \omega_{\text{ph}}/A_c, \quad (\text{B4})$$

with $g_v = 2$ counting the valley degrees of freedom and $A_c = \frac{3\sqrt{3}}{2}a^2$ being the area of unit cell. The prefactor 2 is included to count both electrons and holes. By comparing (B2) and (B4), we have

$$\tau_{\text{ph}}^{-1} = \alpha n_{\text{ex}}, \quad \text{with } \alpha = \frac{\pi g_{\text{ep}}^2 A_c}{2\omega_{\text{ph}}}. \quad (\text{B5})$$

-
- [1] K. S. Novoselov, A. K. Geim, S. V. Morozov, D. Jiang, Y. Zhang, S. V. Dubonos, I. V. Grigorieva, and A. A. Firsov, *Science* **306**, 666 (2004).
- [2] A. C. Neto, F. Guinea, N. M. Peres, K. S. Novoselov, and A. K. Geim, *Rev. Mod. Phys.* **81**, 109 (2009).
- [3] S. Das Sarma, S. Adam, E. H. Hwang, and E. Rossi, *Rev. Mod. Phys.* **83**, 407 (2011).
- [4] J. Moser, A. Barreiro, and A. Bachtold, *Appl. Phys. Lett.* **91**, 163513 (2007).
- [5] I. Meric, M. Y. Han, A. F. Young, B. Ozyilmaz, P. Kim, and K. L. Shepard, *Nat. Nanotechnol.* **3**, 654 (2008).
- [6] A. Barreiro, M. Lazzeri, J. Moser, F. Mauri, and A. Bachtold, *Phys. Rev. Lett.* **103**, 076601 (2009).
- [7] V. E. Dorgan, M.-H. Bae, and E. Pop, *Appl. Phys. Lett.* **97**, 082112 (2010).
- [8] H. Ramamoorthy, R. Somphonsane, J. Radice, G. He, C.-P. Kwan, and J. Bird, *Nano Lett.* **16**, 399 (2015).
- [9] J. Chauhan and J. Guo, *Appl. Phys. Lett.* **95**, 023120 (2009).
- [10] A. M. DaSilva, K. Zou, J. K. Jain, and J. Zhu, *Phys. Rev. Lett.* **104**, 236601 (2010).
- [11] V. Perebeinos and P. Avouris, *Phys. Rev. B* **81**, 195442 (2010).
- [12] T. Fang, A. Konar, H. Xing, and D. Jena, *Phys. Rev. B* **84**, 125450 (2011).
- [13] J. Li, C. Aron, G. Kotliar, and J. E. Han, *Phys. Rev. Lett.* **114**, 226403 (2015).
- [14] C. Zener, *Proc. R. Soc. A* **137**, 696 (1932).
- [15] R. Danneau, F. Wu, M. F. Craciun, S. Russo, M. Y. Tomi, J. Salmilehto, A. F. Morpurgo, and P. J. Hakonen, *Phys. Rev. Lett.* **100**, 196802 (2008).
- [16] H. C. Kao, M. Lewkowicz, and B. Rosenstein, *Phys. Rev. B* **82**, 035406 (2010).
- [17] F. Miao, S. Wijeratne, Y. Zhang, U. C. Coskun, W. Bao, and C. N. Lau, *Science* **317**, 1530 (2007).
- [18] I. V. Oladyshkin, S. B. Bodrov, Y. A. Sergeev, A. I. Korytin, M. D. Tokman, and A. N. Stepanov, *Phys. Rev. B* **96**, 155401 (2017).
- [19] B. Rosenstein, M. Lewkowicz, H. C. Kao, and Y. Korniyenko, *Phys. Rev. B* **81**, 041416 (2010).
- [20] N. Vandecasteele, A. Barreiro, M. Lazzeri, A. Bachtold, and F. Mauri, *Phys. Rev. B* **82**, 045416 (2010).

- [21] G. Kané, M. Lazzeri, and F. Mauri, *J. Phys. Condens. Matter* **27**, 164205 (2015).
- [22] J. Schwinger, *Phys. Rev.* **82**, 664 (1951).
- [23] B. Dóra and R. Moessner, *Phys. Rev. B* **81**, 165431 (2010).
- [24] D. Allor, T. D. Cohen, and D. A. McGady, *Phys. Rev. D* **78**, 096009 (2008).
- [25] F. m. c. Fillion-Gourdeau and S. MacLean, *Phys. Rev. B* **92**, 035401 (2015).
- [26] A. Denis, B. Plaçais, C. Voisin, E. Baudin, G. Zhang, G. Fève, J.-M. Berroir, K. Watanabe, M. Rosticher, Q. Wilmart, *et al.*, *Nat. Nanotechnol.* , 1 (2017).
- [27] J. E. Han, *Phys. Rev. B* **87**, 058119 (2013).
- [28] J. E. Han and J. Li, *Phys. Rev. B* **88**, 075113 (2013).
- [29] J. Li, C. Aron, G. Kotliar, and J. E. Han, *Nano Lett.* (2017).
- [30] E. H. Hwang and S. Das Sarma, *Phys. Rev. B* **77**, 115449 (2008).
- [31] L. Pietronero, S. Strässler, H. R. Zeller, and M. J. Rice, *Phys. Rev. B* **22**, 904 (1980).
- [32] H. Aoki, N. Tsuji, M. Eckstein, M. Kollar, T. Oka, and P. Werner, *Rev. Mod. Phys.* **86**, 779 (2014).
- [33] A. Mitra and A. J. Millis, *Phys. Rev. B* **77**, 220404 (2008).
- [34] R. Shishir, D. Ferry, and S. Goodnick, *Journal of Physics: Conference Series* **193**, 012118 (2009).
- [35] M. Freitag, H.-Y. Chiu, M. Steiner, V. Perebeinos, and P. Avouris, *Nat. Nanotechnol.* **5**, 497 (2010).
- [36] M.-H. Bae, Z.-Y. Ong, D. Estrada, and E. Pop, *Nano Lett.* **10**, 4787 (2010).
- [37] M.-H. Bae, S. Islam, V. E. Dorgan, and E. Pop, *ACS Nano* **5**, 7936 (2011).
- [38] I. J. Luxmoore, C. Adlem, T. Poole, L. Lawton, N. Mahlmeister, and G. R. Nash, *Appl. Phys. Lett.* **103**, 131906 (2013).
- [39] T. E. Beechem, R. A. Shaffer, J. Nogan, T. Ohta, A. B. Hamilton, A. E. McDonald, and S. W. Howell, *Sci. Rep.* **6** (2016).
- [40] D. K. Ferry, *Semicond. Sci. Technol.* **32**, 025018 (2017).
- [41] W. Yang, S. Berthou, X. Lu, Q. Wilmart, A. Denis, M. Rosticher, T. Taniguchi, K. Watanabe, G. Fève, J.-M. Berroir, G. Zhang, C. Voisin, E. Baudin, and B. Plaçais, *Nat. Nanotechnol.* **13**, 47 (2018).
- [42] M. A. Yamoah, W. Yang, E. Pop, and D. Goldhaber-Gordon, *ACS Nano* **11**, 9914 (2017).